Supplementary Information for:

Singlet machine learning photodynamics reveal competing inversion paths of methylated cyclooctatetrathiophene

Christian Salguero and Steven A. Lopez*

Department of Chemistry and Chemical Biology, Northeastern University, Boston, Massachusetts, 02115, United States

*Corresponding author: s.lopez@northeastern.edu

Distribution of S_1/S_0 surface crossings and inversions

Our analysis of our ML-NAMD simulations revealed that each trajectory could undergo several inversions and surface crossing events, irrespective of the final relative stereochemical outcome. To assess the occurrence of surface crossings and inversions within our trajectory ensemble, we quantified the distribution of S_1/S_0 surface crossings and relative stereochemical inversions across all trajectories. We separated the trajectories based on the relative stereochemical product, **MeCOTh-b** (Figure S1a) and **MeCOTh** (Figure S1b). We hypothesize that trajectories leading to the relative stereochemistry of **MeCOTh-b** will undergo one inversion, while those leading to the relative stereochemistry of **MeCOTh** will either undergo two inversions or none at all.

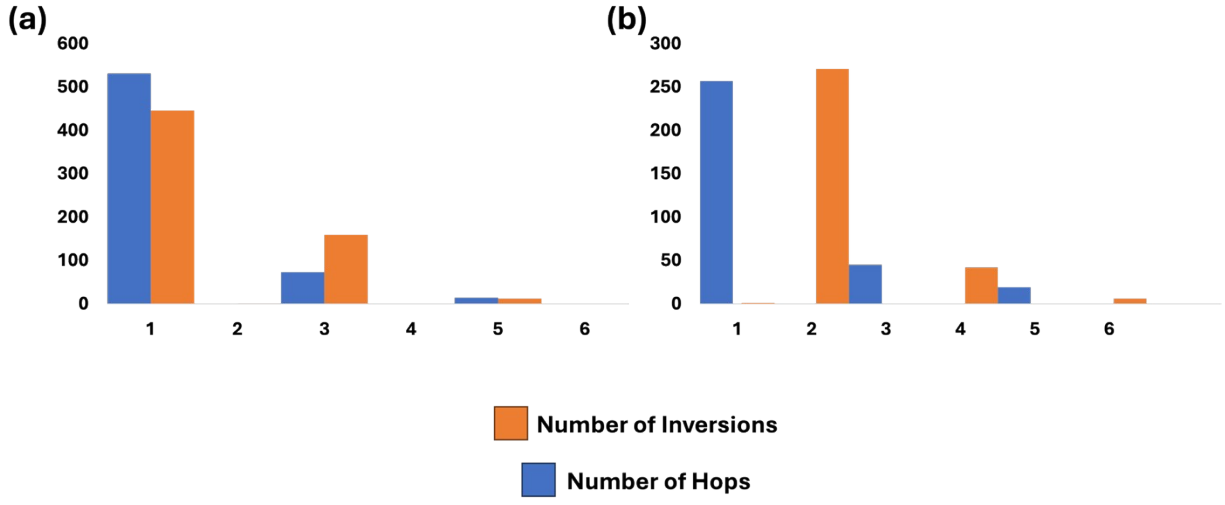

Figure S1. Distribution of the inversions and surface crossing events for trajectories that result in **(a)** the product with inverted relative stereochemistry, **MeCOTh-b**, and **(b)** the product with relative stereochemistry matching that of the reactant, **MeCOTh**.

We observed that 788 trajectories featured one $S_1 \rightarrow S_0$ surface hopping point, irrespective of their final geometry (*i.e.,* **MeCOTh** or **MeCOTh-b**). The remaining 159 trajectories exhibited an odd number of surface hopping events; up to 5 surface crossing

events were possible. We observed that trajectories leading to the inverted product, **MeCOTh-b**, had an odd number (*i.e.,* 1, 3, and 5) of inversions, while those leading to **MeCOTh** had an even number (*i.e.,* 2, 4, and 6). Of the trajectories that led to **MeCOTh-b**, 69% (446) exhibited a single relative stereochemical inversion. This result indicates that while up to five inversions could occur, the dominant mechanistic pathway towards **MeCOTh-b** favored one relative stereochemical inversion. Of the reaction pathways leading to **MeCOTh**, 89% (271) of the trajectories exhibited two relative stereochemical inversions. This result demonstrates that while 6 relative stereochemical inversions are possible, the main mechanistic pathway towards **MeCOTh** predominantly only exhibits 2 inversions. The distributions of the surface crossings and inversions align with our initial hypothesis that most trajectories will have one S_1/S_0 surface hopping point and the minimum inversions towards **MeCOTh-b** (1 inversion) or **MeCOTh** (2 inversions).

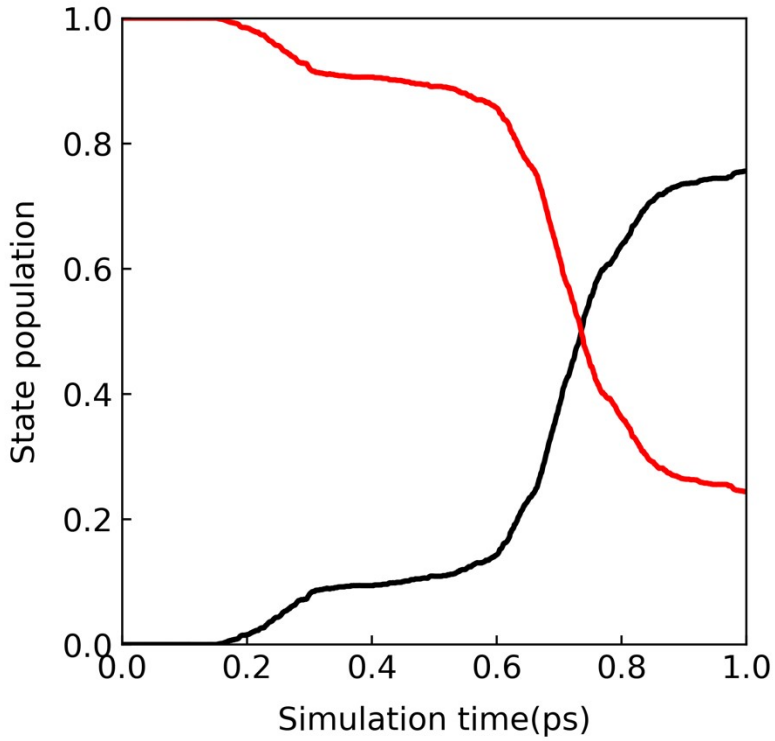

Figure S2. Population map of **MeCOTh** over time in picoseconds (ps) derived from ML-NAMD trajectories propagated by the neural networks trained on SA5-CASSCF(8,7)/ANO-S-VDZP quantum mechanical calculations. The red line denotes the S_1 population, whereas the black line indicates the S_0 population.

The excited state half-life for **MeCOTh** was 736 fs; the corresponding time constant was 1.06 ps.

Minimum Energy Conical Intersection

To explore the structural diversity among the clusters of surface hopping points, we optimized three minimum energy conical intersections (MECIs) for each relative stereochemistry (**MeCOTh** and **MeCOTh-b**), with representative geometries shown in Figure 6 of the main paper. We used the S_1/S_0 hopping points as initial guess structures. We propose that these MECIs will be stereoisomers of the MECIs optimized from the S_1/S_0 hopping points belonging to the intermediate cluster. We hypothesized that trajectories with MECIs exhibiting opposite relative stereochemistries compared to their final geometries might encounter a different conical intersection than those with matching relative stereochemistries. We plotted the θ_{inv} of the last S_1/S_0 surface hopping points against time for all trajectories in Figure S3. We use θ_{inv} to assess the relative stereochemistries of the S_1/S_0 hopping points.

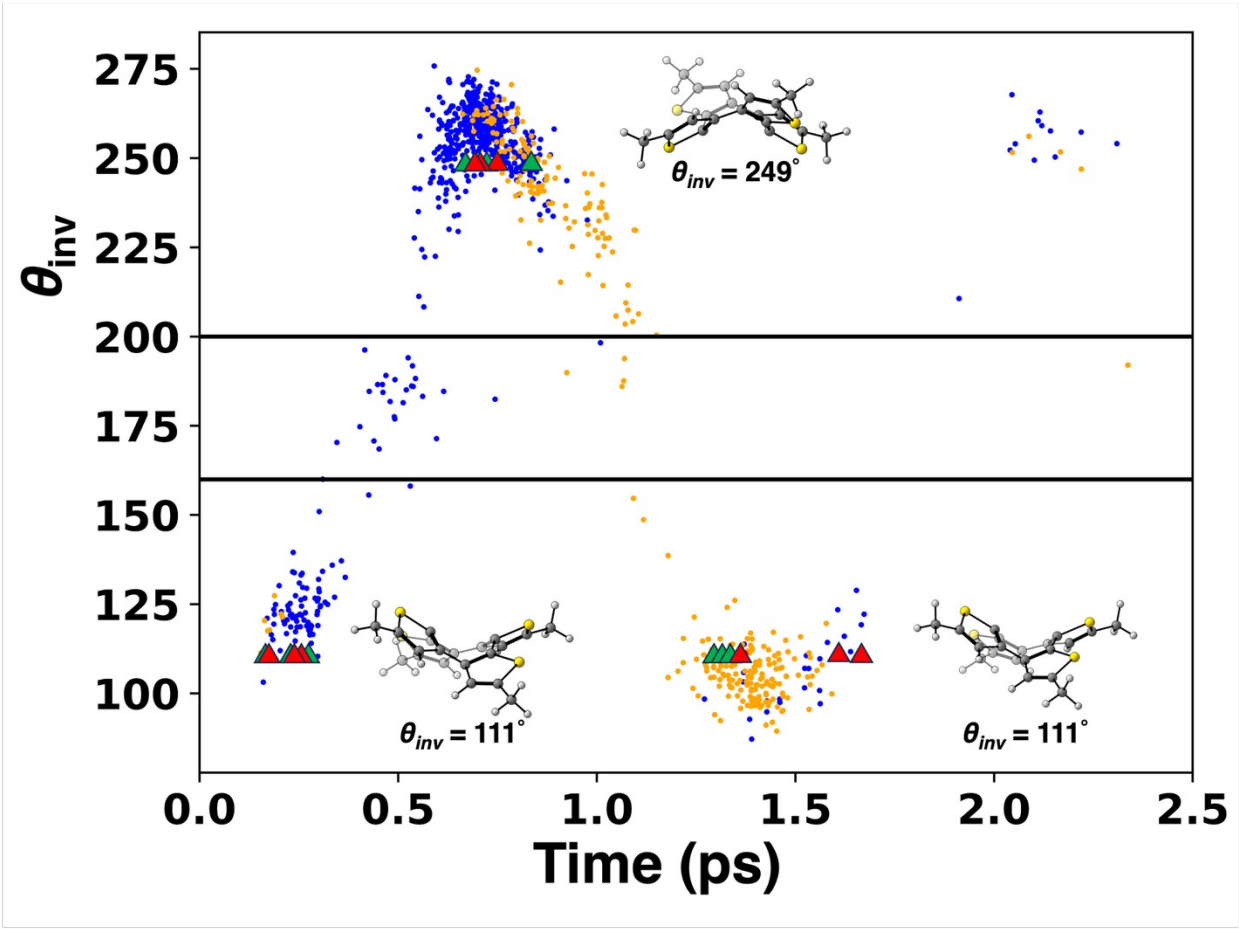

Figure S3. We use color coding for S_1/S_0 hopping points based on their relative stereochemistry, 500 fs after the last $S_1 \rightarrow S_0$ crossing: orange signifies the relative stereochemistry of **MeCOTh**, while blue indicates the relative stereochemistry of **MeCOTh-b**. The red and green triangles mark the positions of minimum energy conical intersections (MECIs), and the solid lines denote the geometric cutoffs for inversions.

We found that all MECIs optimized from S_1/S_0 hopping points belonging to the early and late clusters have a θ_{inv} value of 111°, regardless of the final relative stereochemistries of the trajectories. This θ_{inv} value suggests that the relative stereochemistries of these MECIs correspond to that of **MeCOTh**. In contrast, all MECIs optimized from S_1/S_0 hopping points in the intermediate cluster had θ_{inv} = 249°, irrespective of the final relative stereochemistries. This θ_{inv} value suggest that these MECIs align their relative stereochemistries with **MeCOTh-b**. Regardless of the cluster or the final relative stereochemistry, all MECIs remained at 3.25 eV above **MeCOTh-S_0** (see Table S1).

Table S1. CASSCF(8,7)/ANO-S-VDZP energies of the 18 optimized MECIs, we optimized three MECIs per cluster per relative stereochemical product (**MeCOTh** and **MeCOTh-b**). All energies are presented in eV.

MeCOTh	**MECI-1**	**MECI-2**	**MECI-3**
Early	3.2539	3.2537	3.2538
Intermediate	3.2535	3.2539	3.2539
Late	3.2539	3.2539	3.2535
MeCOTh-b	**MECI-1**	**MECI-2**	**MECI-3**
Early	3.2539	3.2540	3.2539
Intermediate	3.2539	3.2535	3.2539
Late	3.2536	3.2537	3.2540

We observed that the difference between the MECIs belonging to the same cluster arises by the time of appearance rather than in energy or θ_{inv}. To determine whether structural equivalence exists between the optimized MECIs, we compared their bond lengths (π_{CC} and σ_{CC}) within the COT core. The π_{CC} bond lengths of all MECIs are 1.44 Å, 1.45 Å, 1.44 Å, and 1.45 Å. Similarly, all optimized MECIs exhibit σ_{CC} bond lengths of 1.39 Å, 1.39 Å, 1.37 Å, and 1.39 Å. The **MeCOTh-S_1** geometry exhibited comparable π_{CC}/σ_{CC} bond lengths to those of the MECIs, with the four π_{CC} bonds measuring 1.44 Å, 1.45 Å, 1.44 Å, and 1.45 Å, and the four σ_{CC} bonds measuring 1.39 Å, 1.39 Å, 1.37 Å, and 1.40 Å. The same π_{CC}/σ_{CC} bond lengths and common boat-boat conformation seen in all optimized MECIs indicate that MECIs within each cluster are identical. Furthermore, the MECIs optimized from the early/late clusters are stereoisomers of those optimized from the intermediate cluster. The comparable π_{CC}/σ_{CC} bond lengths and shared conformation observed between the MECIs and **MeCOTh-S_1** suggest that these structures occupy similar regions of the potential energy surface. The findings show no alternative MECI in the clusters for trajectories with opposite relative stereochemistries between the S_1/S_0 hopping points and their final geometries. Therefore, an S_0 inversion must take place in these trajectories.

Sulfur – Sulfur Closed Shell Repulsions

We identified two competing pathways for relative stereochemical inversion, driven by different electronic effects: Baird aromaticity and S-S closed-shell repulsions. We monitored the distance between the two pairs of adjacent sulfurs, d_{SS}, within **MeCOTh**. In Figure S4, we plotted the d_{SS} over time, focusing on trajectories that underwent relative stereochemical inversion solely via crown or planar structures. To directly compare with Figure 4 in the main text, we plotted these trajectories until their final S_1/S_0 crossings and extended each trajectory by 500 fs on the S_0 surface *(i.e.,* after the S_1/S_0 hop). In the main text, we proposed that trajectories mainly influenced by S-S closed-shell repulsions exhibit relative stereochemical inversion via a crown geometry, while those predominantly influenced by Baird aromaticity exhibit inversion through a planar geometry. Based on this, we hypothesized that in the trajectory maps highlighting the d_{SS}, the trajectories that pass through the crown structures will have smaller d_{SS} values than those that pass through the planar geometry.

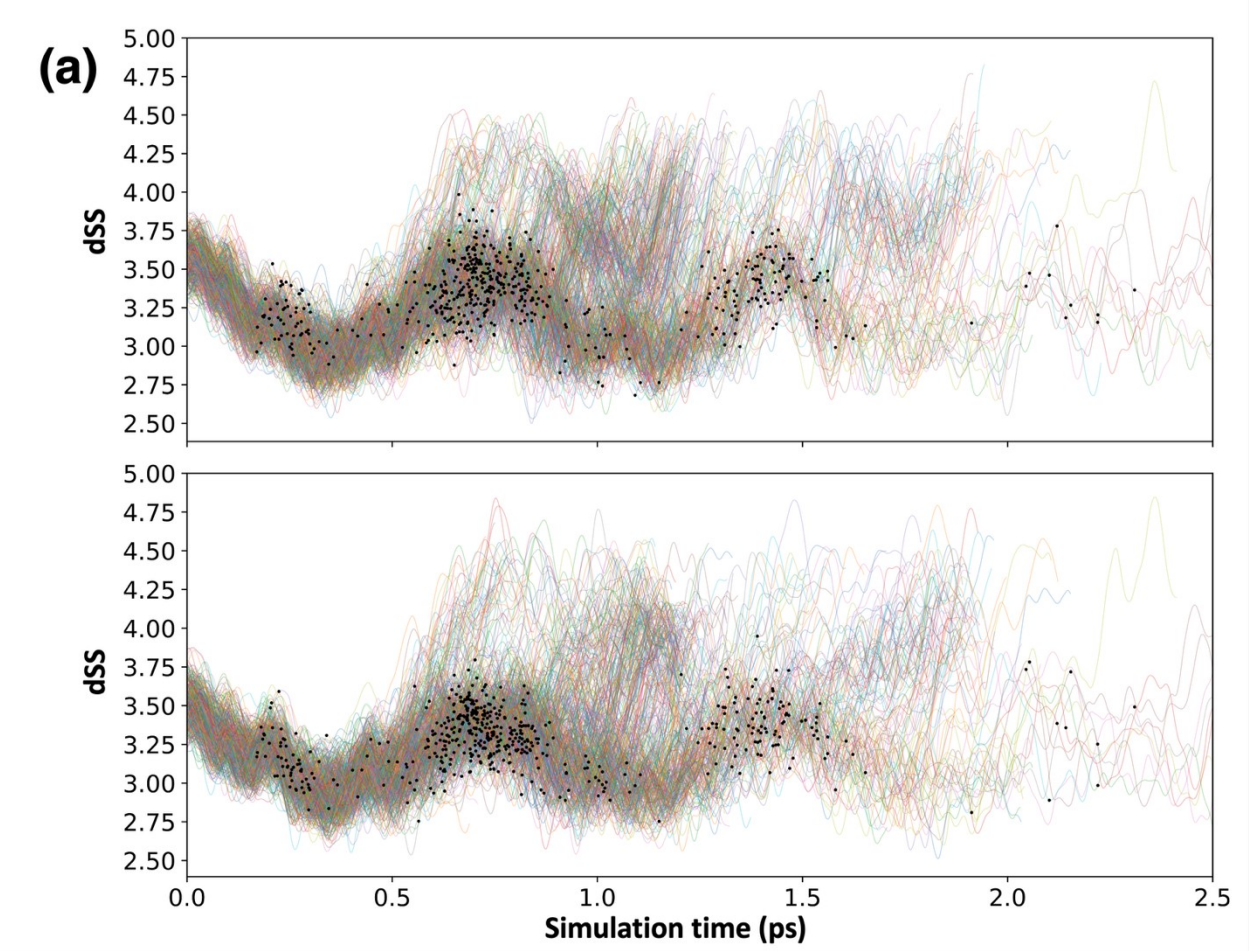

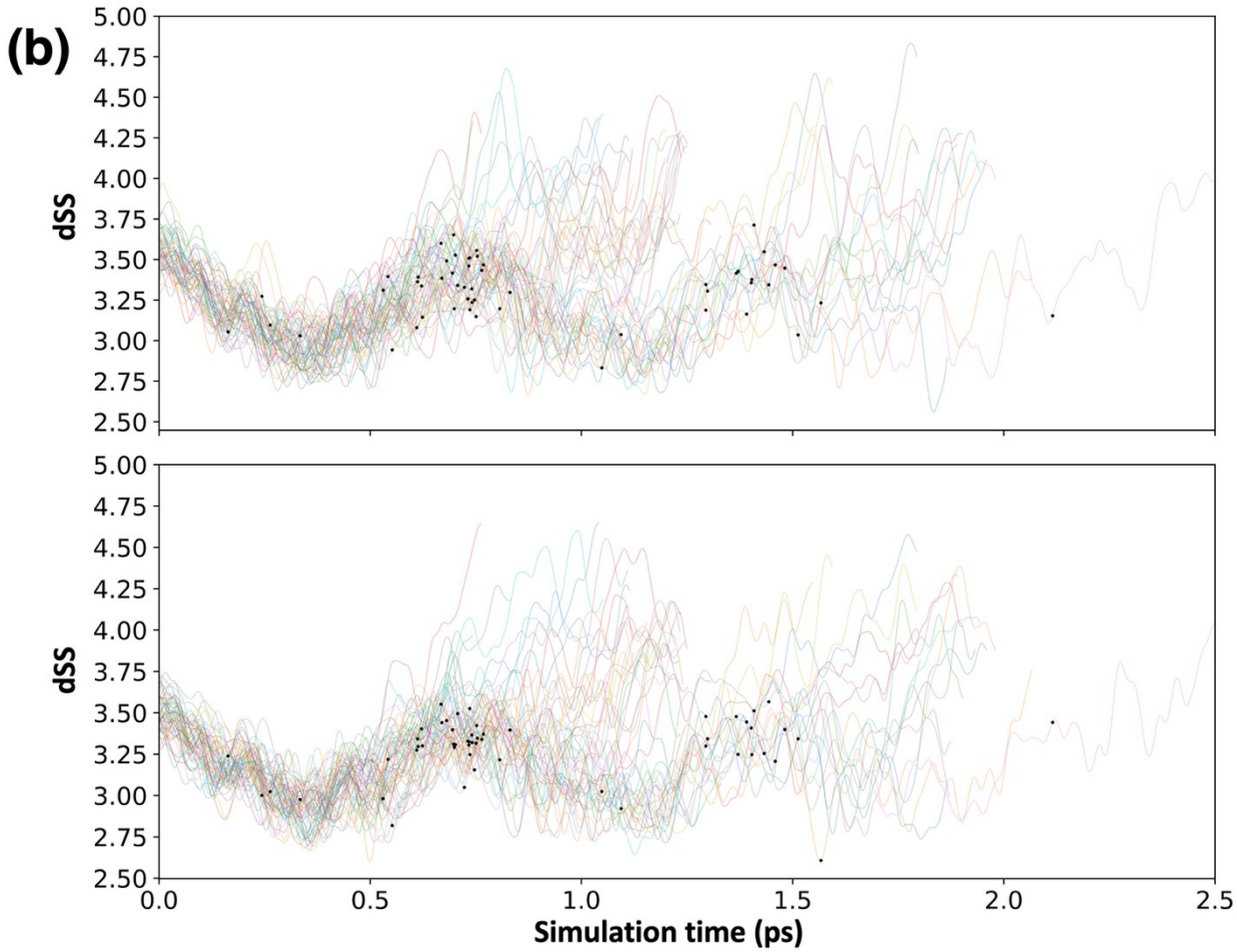

Figure S4. Trajectory map (d_{SS} vs. simulation time) of **MeCOTh → MeCOTh-b** inversion. We separated the trajectories based on the reaction pathway they proceeded through: **(a)** crown vs. **(b)** planar. We tracked geometries of the trajectories 500 fs after the S_1/S_0 crossing. Black dots represent S_1/S_0 surface hopping points.

The planar transition state structure presented by Ueda *et al.* has a d_{SS} of 2.85 Å; at this d_{SS} value, the sulfur-sulfur closed-shell repulsive interactions are expected to be at a maximum. Therefore, we used this d_{SS} value as a threshold within our trajectory maps to measure the degree of S-S closed-shell repulsions. We found that 70% of trajectories that undergo relative stereochemical inversion via the crown geometry passed the d_{SS} threshold. In comparison, 62% of trajectories that underwent the relative stereochemical inversion through the planar geometry passed the d_{SS} threshold. Based on these results, we conclude that trajectories passing through the crown geometry experience increased S-S closed-shell repulsive interactions. In contrast, those that passed through the planar geometry experienced decreased S-S closed-shell repulsions. These findings align with our initial reasoning for the crown formation and dominance in the mechanistic pathways.

Grid Search and Hyperparameter Optimization

To determine the optimal hyperparameters, we performed a grid search across several parameters, including the number of hidden layers (3 to 7), nodes per hidden layer (200 to 800), batch sizes (64 or 128), and L2 regularization factors (10^{-7}, 10^{-8}, and 10^{-9}), which involved 210 NNs. The optimized hyperparameters are shown in Table S2.

Table S2. Training setup and hyperparameters of the NN potentials for **MeCOTh.**

Data Size	2560	
Activation Function	Leaky softplus	
Training : Validation	9:1	
$Loss_{Energy}$: $Loss_{Force}$	5:1	
Model	**NN1**	**NN2**
Layers	4	4
Nodes	600	700
Batch Size	64	64
L2 regularization	10^{-8}	10^{-8}
Steps for learning rate of 10^{-3}	600	600
Steps for learning rate of 10^{-4}	300	300
Steps for learning rate of 10^{-5}	100	100

Nuclear independent chemical shift calculations on S_0 and T_1 surfaces

We attempted to implement S_1 NICS(1) (*i.e.,* CASSCF(8,7)/6-31(d,p)) using the Dalton program[1] to provide a more in-depth analysis of the differences in aromatic character between the **MeCOTh** geometries in different surfaces (*i.e.,* **MeCOTh-S_0**, **MeCOTh-S_1**, **1-MEP-8**, **MeCOTh-MECI-intermediate**, planar, and crown). However, calculating NICS(1) on the S_1 surface for **1-MEP-11** proved computationally expensive; the calculation remained on the SIRIUS module (*i.e.,* the wavefunction computation module) after a 7-day run on one node with 16 processors.

Ueda *et al.* observed that the acceleration of the relative stereochemical inversion of **MeCOTh** occurred in both the S_1- and T_1-surfaces.[2] Therefore, we can circumvent the computational cost of S_1 NICS(1) by running T_1 NICS(1) calculations using the Gaussian16 software.[3] To this end, we calculated the S_0 NICS(1) and T_1 NICS(1) values for key mechanistic geometries of **MeCOTh** along the two competing pathways—those facilitated by the planar and crown structures—using B3LYP/aug-cc-pVTZ and UB3LYP/aug-cc-pVTZ, respectively. We hypothesize that structures with a more planar geometry, (*e.g.,* **1-MEP-11**, and **MeCOTh-MECI-intermediate)** will adhere to Hückel's and Baird's rules of aromaticity—being Hückel antiaromatic in the S_0 state and Baird aromatic in the T_1 state. We summarized the results of the key geometries (Figure S5): **MeCOTh-S_0**, **MeCOTh-S_1**, **1-MEP-11**, **MeCOTh-MECI-intermediate**, **MeCOTh-planar**, and **MeCOTh-crown** geometry in Table S3.

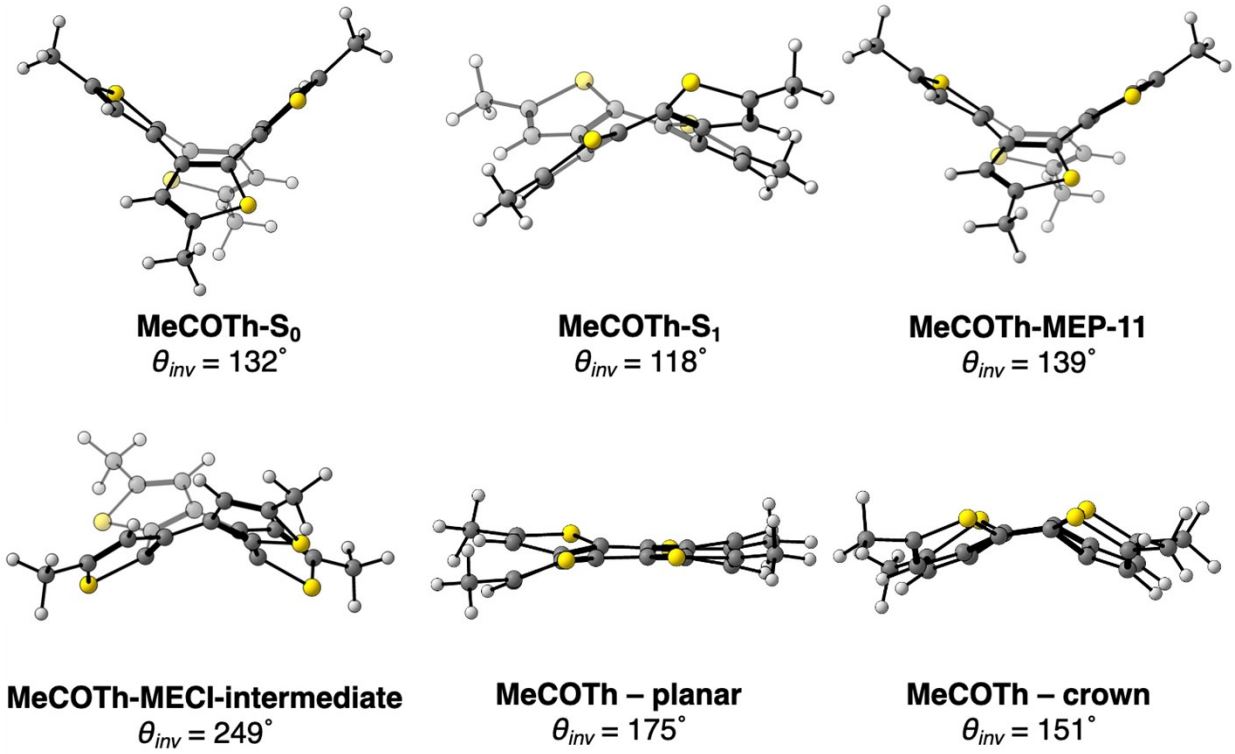

Figure S5. Key mechanistic geometries identified in our ML-NAMD trajectories: **MeCOTh-S_0**, **MeCOTh-S_1**, **1-MEP-11**, **MeCOTh-MECI-intermediate**, **MeCOTh-planar**, and **MeCOTh-crown**, with their respective θ_{inv} below each structure.

Table S3. All calculated B3LYP/aug-cc-pVTZ and UB3LYP/aug-cc-pVTZ NICS(1) values for key geometries of **MeCOTh** along the two competing pathways on the S_0- and T_1-surfaces, respectively.

Geometry	S_0 NICS(1)	T_1 NICS(1)
MeCOTh-S_0	-0.51	-3.96
MeCOTh-S_1	41.88	-9.23
1-MEP-11	6.04	-8.05
MeCOTh-MECI-intermediate	27.42	-8.42
MeCOTh-planar	65.15	-9.01
MeCOTh-crown	784.58	-8.57

We evaluated the S_0 NICS(1) and T_1 NICS(1) at mechanistic critical points to assess changes in aromaticity along geometries commonly encountered in the competing **MeCOTh** → **MeCOTh-b** pathways. A negative NICS(1) value less than -5 ppm indicates aromaticity, while a positive NICS(1) value greater than 5 ppm suggests antiaromaticity.[4, 5] NICS(1) values that fall within -5 ppm and 5 ppm indicate nonaromaticity.[4, 5] The S_0 NICS(1) values were -0.51 ppm, 41.88 ppm, 6.04 ppm, 27.42 ppm, 65.15 ppm, and 784.58 ppm for **MeCOTh-S_0**, **MeCOTh-S_1**, **1-MEP-11**, **MeCOTh-MECI-intermediate**, **MeCOTh-planar**, and **MeCOTh-crown** geometry, respectively. **MeCOTh-S_0** was the only

geometry with a negative NICS(1) value (-0.51 ppm) in the S_0 state; the small NICS(1) value (*i.e.,* -5 ppm <) indicates nonaromaticity rather than aromaticity. We attributed the nonaromatic nature of **MeCOTh-S_0** to the tub-geometry, which disrupts the π-conjugation needed for aromaticity/antiaromaticity. All other geometries (*i.e.,* **MeCOTh-S_1**, **1-MEP-11**, **MeCOTh-MECI-intermediate**, **MeCOTh-planar**, and **MeCOTh-crown**) had positive NICS(1) values greater than 5 ppm on the S_0 surface, indicating that these structures were Hückel antiaromatic. The S_0 NICS(1) values increased in the following order: **1-MEP-11** (6.04 ppm), **MeCOTh-MECI-intermediate** (27.42 ppm), **MeCOTh-S_1** (41.88 ppm), **MeCOTh-planar** (65.15 ppm), and **MeCOTh-crown** (784.58 ppm). According to the conventional interpretation[5] of NICS values, the most antiaromatic on the S_0 state was **MeCOTh-crown**, followed by **MeCOTh-planar** and **MeCOTh-S_1**. This aligns with Hückel's rules of aromaticity: the more conjugated a 4n π electron system is on the S_0 surface, the more antiaromatic it becomes. Based on these results, we hypothesize that the aromaticity would be highest in the T_1 state for the **MeCOTh-planar**, **MeCOTh-crown**, and **MeCOTh-S_1** structures.

On the T_1 surface, all NICS(1) values were negative, indicating that these structures were Baird aromatic. The T_1 NICS(1) values were in the following increasing order: **MeCOTh-S_1** (-9.23 ppm), **MeCOTh-planar** (-9.01 ppm) < **MeCOTh-crown** (-8.57 ppm) < **MeCOTh-MECI-intermediate** (-8.42 ppm) < **1-MEP-11** (-8.05 ppm) < **MeCOTh-S_0** (-3.96 ppm). Similar to the S_0 NICS(1) value for **MeCOTh-S_0**, the T_1 NICS(1) value for **MeCOTh-S_0** also falls within the nonaromatic window (-5 ppm < x < 5 ppm). The most aromatic structure on the T_1 surface was **MeCOTh-S_1** (-9.23 ppm), followed by **MeCOTh-planar** (-9.01 ppm) and **MeCOTh-crown** (-8.75 ppm). This aligns with our initial hypothesis, as the S_0 NICS(1) and T_1 NICS(1) values for the **MeCOTh-planar** (65.15 ppm vs -9.01 ppm, respectively), **MeCOTh-crown** (784.48 ppm vs -8.57 ppm), and **MeCOTh-S_1** (41.88 ppm vs -9.23 ppm, respectively) exchange parity based on their respective surfaces. The positive NICS(1) values on the S_0 surface indicate that the **MeCOTh-planar**, **MeCOTh-crown**, and **MeCOTh-S_1** geometries are Hückel antiaromatic. In contrast, the negative NICS(1) values on the T_1 state signify that these structures are Baird aromatic. The increase in the S_0 NICS(1) and T_1 NICS(1) values from **MeCOTh-S_0** (-0.51 ppm and -3.96 ppm, respectively) → **1-MEP-11** (6.04 ppm vs -8.05 ppm, respectively) aligns with our initial assessment of increased Baird aromaticity along the excited state minimum energy path. Additionally, the S_0 NICS(1) and T_1 NICS(1) values support our hypothesis that S-S closed-shell repulsion outcompetes the benefits of Baird aromaticity in the twisted COT-core structures (like **MeCOTh-crown** and **MeCOTh-S_1**), since these structures show antiaromatic and aromatic NICS(1) values, respectively, without the planar geometry associated with aromaticity. The agreement between the S_0 NICS(1) and T_1 NCIS(1) values (*i.e.,* parity exchange) shows that these methods accurately describe the aromatic/antiaromatic electronic configuration of the **MeCOTh** geometries, but the high S_0 NICS(1) value of **MeCOTh-crown** (784.58 ppm) indicates that NICS should not be used as a quantitative measure of aromaticity for **MeCOTh**.

To complement our calculated NICS values, we calculated the harmonic oscillator model of aromaticity – computational (HOMAc)[6] and anisotropy-induced current density (AICD)[7] for all geometries: **MeCOTh-S_0**, **MeCOTh-S_1**, **MeCOTh-MEP-11**, **MeCOTh-MECI-intermediate**, **MeCOTh-planar**, and **MeCOTh-crown** (Table S4 and Figure S6a-f,

respectively). A HOMAc value of -1 represents antiaromaticity, while a value of 1 indicates aromaticity; values between -0.5 and 0.5 signify nonaromaticity.[4, 6] In the AICD plots, a diatropic (clockwise) ring current indicates aromaticity, while a paratropic (counterclockwise) ring current indicates antiaromaticity. We expect the HOMAc value for **MeCOTh-S_0** to be within the nonaromaticity range and not display a distinct current. In contrast, the HOMAc values for the other structures—**MeCOTh-S_1**, **MeCOTh-MEP-11**, **MeCOTh-MECI-intermediate**, **MeCOTh-planar**, and **MeCOTh-crown**—are anticipated to be above 0.5 as the geometric index does not consider the PES, showing a diatropic current on the S_0 surface and a paratropic current on the T_1 surface. We have summarized the HOMAc in Table S4 and demonstrated the AICD plots in Figure S6.

Table S4. All calculated harmonic oscillator model of aromaticity – computational (HOMAc) values for key geometries of **MeCOTh** along the two competing pathways.

Geometry	HOMAc
MeCOTh-S_0	0.446
MeCOTh-S_1	0.772
1-MEP-11	0.931
MeCOTh-MECI-intermediate	0.773
MeCOTh-planar	0.570
MeCOTh-crown	0.733

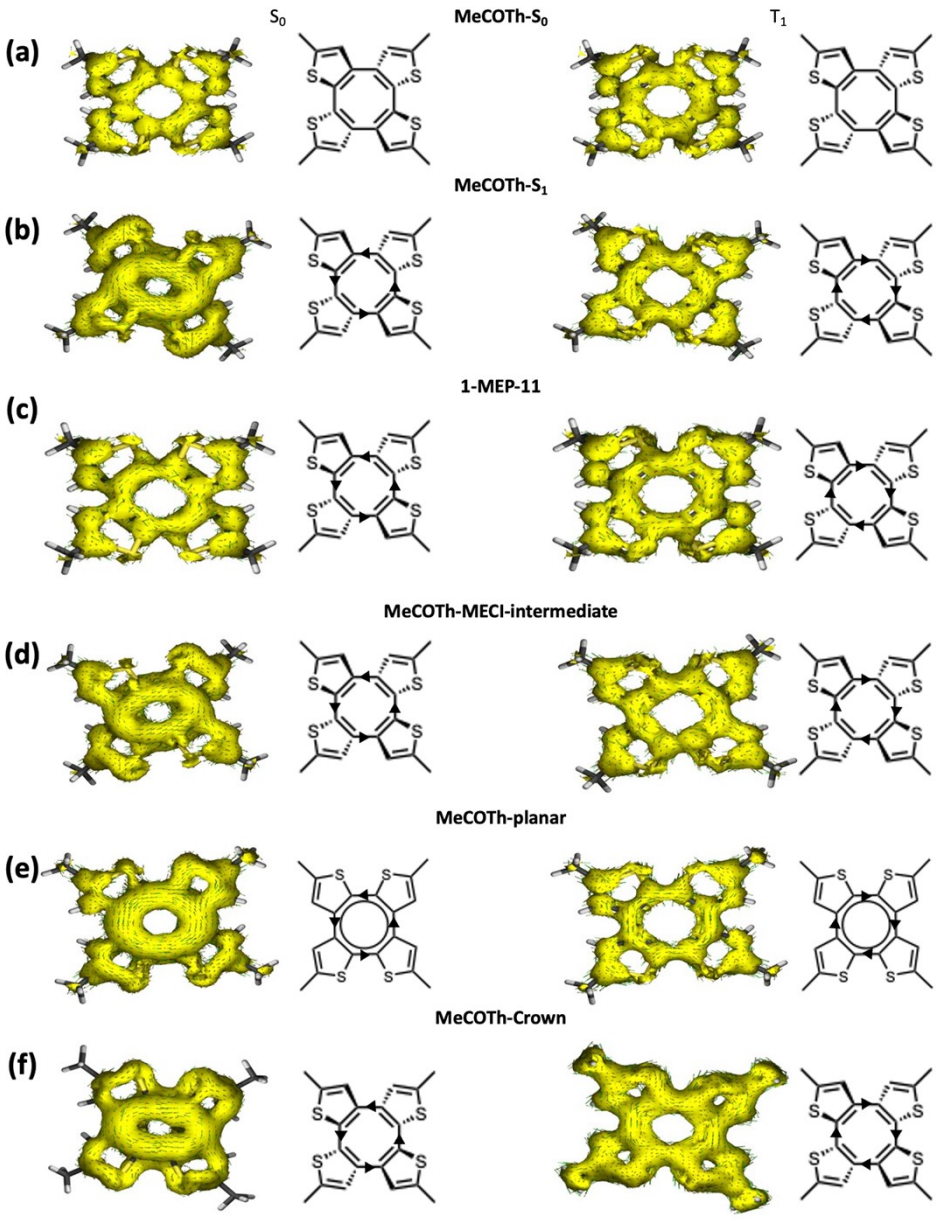

Figure S6. Anisotropy induced current density (AICD) plots for the (a) **MeCOTh-S_0** (saddle), (b) **MeCOTh-S_1**, (c) **MeCOTh-MEP-11**, (d) **MeCOTh-MECI-intermediate**, (e) **MeCOTh-planar**, and (f) **MeCOTh-crown**.

The NICS values for **MeCOTh-S_0** in the S_0 and T_1 states were -0.51 and -3.96 ppm, respectively, indicating that **MeCOTh-S_0** has a nonaromatic electronic structure on the S_0 and T_1 surfaces. The HOMAc value of 0.446 for **MeCOTh-S_0** suggests a nonaromatic electronic structure, consistent with the calculated NICS value. The AICD plots for this structure showed no current. Both the magnetic and geometric indices indicate that **MeCOTh-S_0** has a nonaromatic electronic structure. The remaining structures: **MeCOTh-**

S_1, **MeCOTh-MEP-11**, **MeCOTh-MECI-intermediate**, **MeCOTh-planar**, and **MeCOTh-crown** had S_0 NICS values of 41.88, 6.04, 27.42, 65.15, 784.58 ppm, respectively. In contrast, these structures had T_1 NICS values of -9.23, -8.05, -8.42, -9.01, -8.57 ppm. These NICS values indicated that these structures were Hückel antiaromatic in the S_0 state and Baird aromatic in the T_1 state. The HOMAc values for these structures were 0.772, 0.931, 0.773, 0.570, and 0.733, respectively. All these HOMAc values exceed 0.5, indicating that these structures exhibit an aromatic electronic structure at these excited-state geometries. In Figure S7, all remaining structures (*i.e.,* except for **MeCOTh-S_0**) exhibit diatropic ring currents in the S_0 state and paratropic ring currents on the T_1 surface, indicating Hückel antiaromaticity and Baird aromaticity, respectively. The HOMAc values, AICD plots, and NICS values agree across all structures, confirming our initial NICS analysis.

Momentum analysis of S_1/S_0 hopping points

To evaluate whether the momentum of the thiophene rings (Figure S7a) influences the retention or loss of relative stereochemistries between the S_1/S_0 hopping points and the final geometries, we defined an out-of-plane momentum component, $p_\perp$, based on the atoms within the rings (Figure S7b). We plotted the $p_\perp$ values for all four thiophene rings over time in Figure S7c.

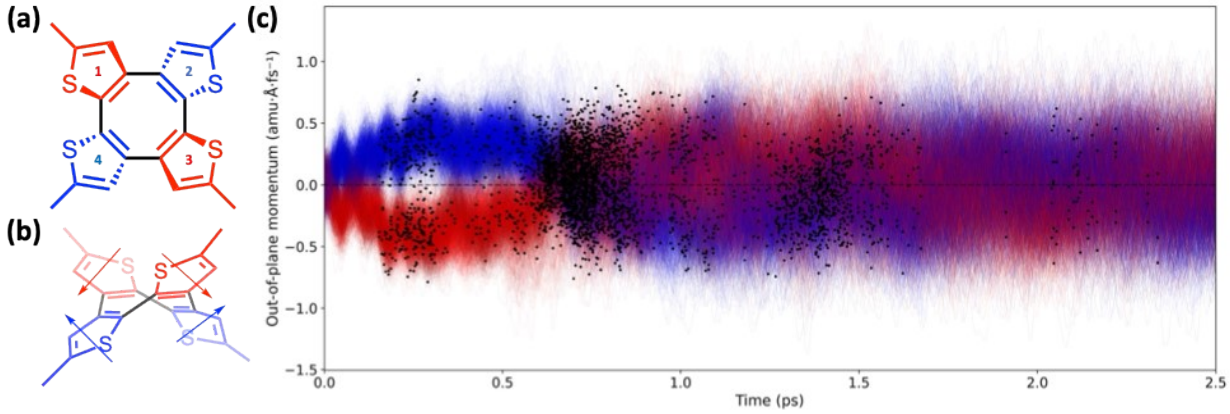

Figure S7. **(a)** The initial **MeCOTh** structure with the thiophene differentiated by the orientation. The two thiophenes initially pointing downward are highlighted in blue, while those pointing upward are highlighted in red. **(b)** The definition of the out-of-plane momentum ($p_\perp$) of the four thiophene rings in **MeCOTh**. **(c)** The $p_\perp$ of the four thiophene rings plotted against time (individual lines), color-coded based on the initial orientation of the thiophene. Each black mark indicates the last S_1/S_0 hopping point for each trajectory.

In Figure S7c, $p_\perp$ values are plotted against time; negative $p_\perp$ values indicate downward movement, while positive $p_\perp$ values indicate upward movement. Rings 1 and 3 show a decrease from 0 to below -0.5 amu Å fs^{-1} within 500 fs, reflecting downward

motion. Conversely, rings 2 and 4 increase from 0 to above 0.5 amu Å fs^{-1}, indicating upward movement. The observed rise in momenta for both pairs of rings indicates that **MeCOTh** is undergoing inversion and moving toward a planar geometry (*i.e.,* all thiophene rings will be coplanar). In Figure 5 of the main paper, we identified three clusters of hopping points at 0–0.5 ps, 0.501–1 ps, and above 1.01 ps. These were labeled by timing as "early," "intermediate," and "late." We determined that 92% of trajectories that pass through the S_1/S_0 hopping point in the early cluster do not retain the relative stereochemistry of the hopping point at the end of the respective trajectory (*i.e.,* inversion occurs). In contrast, those in the intermediate and late clusters do (83% and 84%, respectively).

In Figure S7c, we observe that trajectories that undergo S_1/S_0 hopping points within the early cluster have momentum exceeding ±0.5 amu Å fs^{-1} in their respective direction; this high momentum enables them to complete the relative stereochemical inversion on the ground state. Trajectories that experienced the S_1/S_0 hopping points within the intermediate (0.501-1 ps) and late cluster (beyond 1.01 ps) intervals exhibited a range of $p_\perp$ values (*i.e.*, 0 – 0.5 amu Å fs^{-1}). Within the intermediate and late time windows, we observed that trajectories begin with lower $p_\perp$ values (< 0.5 amu Å fs^{-1}) without undergoing a parity change, then either increase or decrease to ±0.5 amu Å fs^{-1} and reverse their direction. This indicates that S_1/S_0 hopping points occurring earlier in these time windows, during the first half, are associated with lower momentum (less than 0.5 amu Å fs^{-1}) and do not change direction. In contrast, those that occur later are associated with increased momentum (*i.e.,* 0.5 amu Å ps^{-1} <) and change direction. Consequently, trajectories that undergo the S_1/S_0 hop earlier within the given time frames either lack or have insufficient momentum to experience a second relative stereochemical inversion on the S_0 surface. This results in the preservation of the stereochemistries between the S_1/S_0 hops and the final geometries. In contrast, the S_1/S_0 hops that have increased in momentum (*i.e.,* later S_1/S_0 hopping points) within the clusters lead to the second relative stereochemical inversion of **MeCOTh** on the S_0 state (*i.e.,* no retention of relative stereochemistries). Based on these results, the S_0-inversions are attributed to the momentum of the trajectories, rather than to an alternative S_1/S_0 hopping geometry.

Geodesic interpolation from crown-to-planar structures

To provide energetic evidence for the preference of the crown over the planar geometry in the trajectories and investigate the energetic landscape bridging these two geometries, we interpolated 20 structures (**MeCOTh-Int*n***, with ***n*** ranging from 1 to 20) between the crown structure shown in Figure 9 (at 370 fs) and the planar structure depicted in Figure 7 (at 337 fs). We calculated the single point energy of each of these structures using SA5-CASPT2(8,7)/ANO-S-VDZP//SA5-CASSCF(8,7)/ANO-S-VDZP. We compiled all the calculated energy values and measured the distance between the adjacent sulfurs, d_{SS1} and d_{SS2}, in Figure S8. We hypothesize that the crown structure would be lower in energy than the planar geometry on the S_1 surface by maximizing the distance between the sulfurs, which would explain its observed dominance in the mechanistic pathways.

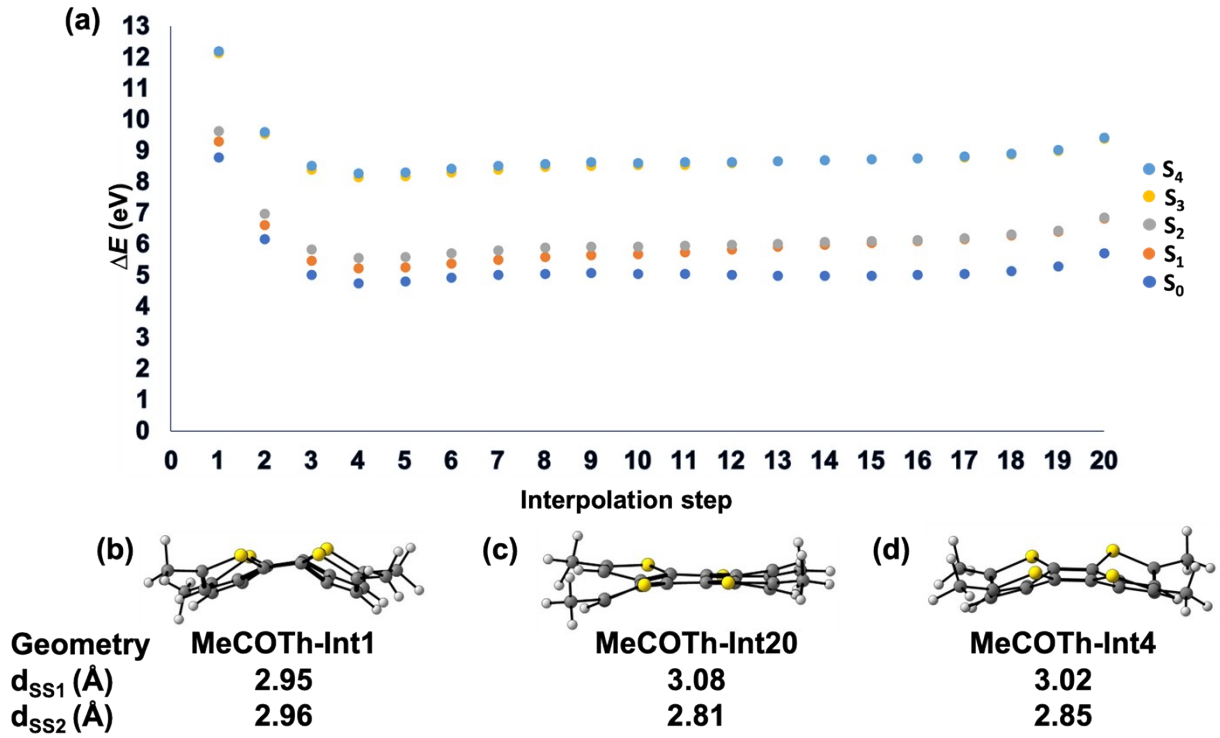

Figure S8. (a) SA5-CASPT2(8,7)/ANO-S-VDZP//SA5-CASSCF(8,7)/ANO-S-VDZP single-point energies along the interpolated path between the crown (**MeCOTh-Int1**) and the planar (**MeCOTh-Int20**). (b) The starting crown structure: **MeCOTh-Int1** (from Figure 7, timestep 337), used for interpolation. (c) The ending planar structure: **MeCOTh-Int20** (from Figure 9, timestep 370), used for interpolation. (d) An intermediate structure, **MeCOTh-Int4**, which has the lowest S_1 energy.

In Figure S8a, we observe that the energy along the S_1 surface of the interpolated pathway starts at 9.32 eV (**MeCOTh-Int1**, Figure S8b) and ends at 6.82 eV (**MeCOTh-Int20**, Figure S8c), corresponding to the crown and planar geometry, respectively. We measured d_{SS1} of 2.95 Å and 3.08 Å and d_{SS2} of 2.96 Å and 2.85 Å for **MeCOTh-Int1** and **MeCOTh-Int20**, respectively. The S_1 energies calculated for **MeCOTh-Int1** and **MeCOTh-Int20** differ by 2.50 eV, while the d_{SS1} and d_{SS2} differ by 0.13 Å and -0.14 Å. The electronic energies indicate that **MeCOTh-Int20** is more stable than **MeCOTh-Int1** on the S_1 surface despite the decreased d_{SS2}. The improved stability of **MeCOTh-Int20** arises from its planar geometry, which enhances π-orbital overlap and amplifies the stabilizing effects of Baird aromaticity and the increased d_{SS1}, outcompeting the destabilizing effects of the S-S closed-shell repulsions from d_{SS2}. This contradicts our hypothesis that the crown structure would be the more stable of the two structures. However, between **MeCOTh-Int1** and **MeCOTh-Int20**, we observed that the fourth structure (**MeCOTh-Int4**, Figure S8d) has an S_1 energy of 5.23 eV with a d_{SS1} and d_{SS2} value of 3.02 Å and 2.85 Å. This structure exhibits a lower S_1 energy compared to **MeCOTh-Int1** and **MeCOTh-Int20**; in fact, it has the lowest S_1 energy among all intermediate structures along the interpolated pathway. Based on these energy values, we notice a 4.09 eV decrease from **MeCOTh-Int1** to **MeCOTh-Int4**, followed by a

consistent rise of 1.59 eV from **MeCOTh-Int4** to **MeCOTh-Int20**. Meanwhile, d_{SS1} increased by 0.7 Å, while d_{SS2} declined by 0.11 Å from **MeCOTh-Int1** to **MeCOTh-Int4**. Subsequently, between **MeCOTh-Int4** and **MeCOTh-Int20**, d_{SS1} rose by 0.06 Å and d_{SS2} dropped by 0.04 Å. The crown structure (**MeCOTh-Int1**) exhibits comparatively high S_1 energy at 9.32 eV due to suboptimal π-orbital overlap and S-S closed-shell repulsion. Conversely, the planar geometry (**MeCOTh-Int20**) exhibits optimal π-orbital overlap; however, it continues to experience S-S closed-shell repulsion from the S-S pair described by d_{SS2}, resulting in an S_1 energy of 6.82 eV. The lowest S_1 energy of 5.23 eV of **MeCOTh-Int4** results from the effective combination of the benefits of the crown (less S-S closed-shell repulsion) and planar (Baird aromaticity) geometries. In conclusion, although the planar structure (**MeCOTh-Int20**) is more stable than the crown geometry (**MeCOTh-Int1**), there is an intermediate (**MeCOTh-Int4**) that is even more stable than both structures on the S_1 surface. This intermediate structure features unidirectional sulfurs and is more planar than **MeCOTh-Int1**, balancing the advantages of Baird aromaticity with ideal S-S distances (*i.e.,* d_{SS1} = 3.02 Å and dSS2 = 2.85 Å) to avoid S-S closed-shell repulsive interactions. This agrees with the report by Ueda *et al.*, who suggest that the quasi-planar geometry of the optimized transition state structure on the S_1 surface results from a balance between S-S closed-shell repulsion and Baird aromaticity.[2] These findings reinforce our main conclusion: Baird aromaticity and S-S closed-shell repulsions are competing electronic effects that affect the stereochemical inversion between **MeCOTh** and **MeCOTh-b.**

Summary of key static structures

To summarize the **MeCOTh**-to-**MeCOTh-b** relative stereochemical inversion mechanism, we have compiled the key geometries: **MeCOTh***, **MeCOTh-MEP-11**, **MeCOTh-S_1**, and MECIs into a reaction coordinate diagram, Figure S9.

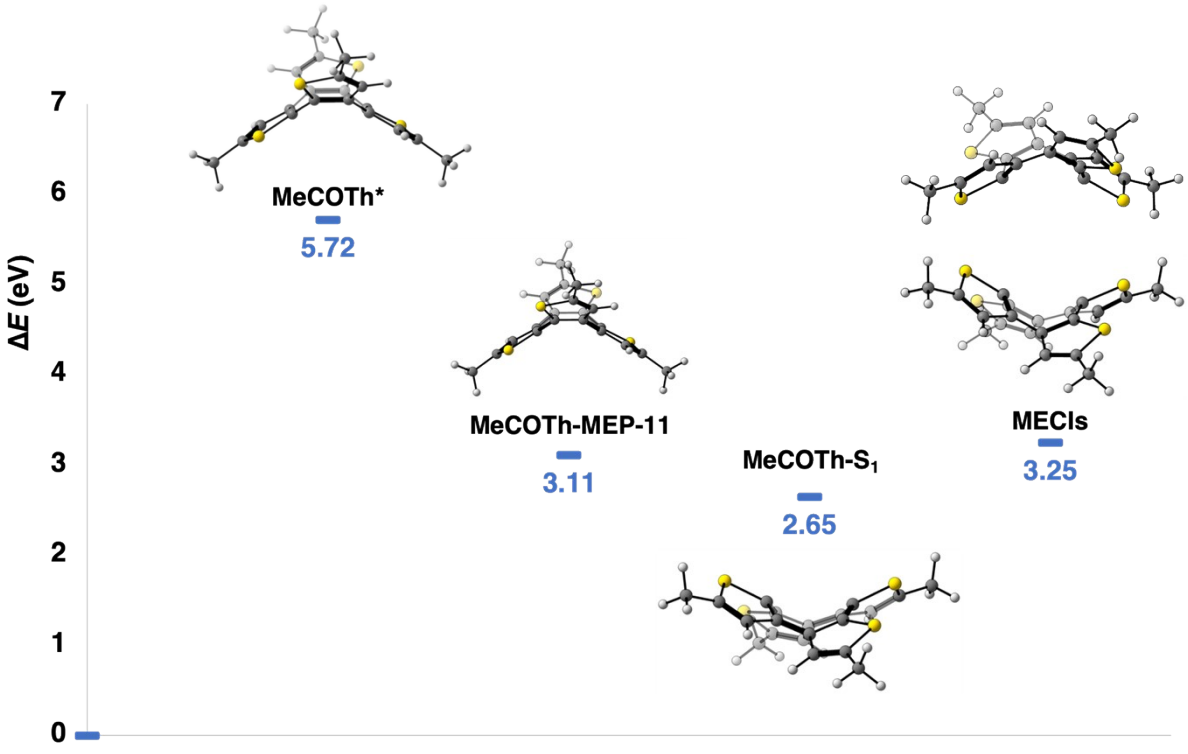

Figure S9. SA5-CASPT2(8,7)/ANO-S-VDZP//CASSCF(8,7)/ANO-S-VDZP reaction coordinate of **MeCOTh**-to-**MeCOTh-b** along S_1-surface. All energies are in eV and are relative to **MeCOTh-S_0.**

The initial step of the photochemical inversion is the photon absorption towards the S_1 surface. We calculated that **MeCOTh** has an S_0-to-S_1 electronic transition of 5.72 eV (*i.e.,* **MeCOTh***). We investigated the path of steepest descent from the Franck-Condon point using a minimum energy path (MEP) calculation and observed that the MEP converged in 11 steps (*i.e.,* 11 intermediate geometries). The final structure, **MeCOTh-MEP-11**, was slightly more planarized than **MeCOTh*** and exhibited an S_1/S_0 energy gap of 2.74 eV and was 3.11 eV above the **MeCOTh-S_0**. Due to the large S_1/S_0 gap, we used it as the initial guess to optimize the S_1 minimum, **MeCOTh-S_1**, which is 2.65 eV higher in energy than **MeCOTh-S_0**. All the structures previously mentioned provide a static perspective of **MeCOTh** on the S_1 surface. However, to provide an insight into the relative stereochemical inversion mechanism, we utilized our machine-learning nonadiabatic molecular dynamics. As such, we trained the ML model using geodesic interpolation and propagated 988 ML-NAMD trajectories. We used the S_1/S_0 hopping points from these trajectories to calculate the minimum energy conical intersections, all of which were 3.25 eV above **MeCOTh-S_0**. We also identified two common structures in the relative stereochemical inversion across the trajectories: **MeCOTh-planar** and **MeCOTh-crown**. Within these trajectories, we observed racemization via the **MeCOTh-planar** and

MeCOTh-crown geometries, after which the trajectories adopted the **MeCOTh-S_1** geometry and subsequently proceeded to an S_1/S_0 hop resembling the MECIs.

References

(1) Aidas, K.; Angeli, C.; Bak, K. L.; Bakken, V.; Bast, R.; Boman, L.; Christiansen, O.; Cimiraglia, R.; Coriani, S.; Dahle, P.; et al. The Dalton quantum chemistry program system. *WIREs Computational Molecular Science* **2014**, *4* (3), 269-284. DOI: https://doi.org/10.1002/wcms.1172 (acccessed 2025/08/22).

(2) Ueda, M.; Jorner, K.; Sung, Y. M.; Mori, T.; Xiao, Q.; Kim, D.; Ottosson, H.; Aida, T.; Itoh, Y. Energetics of Baird aromaticity supported by inversion of photoexcited chiral [4n]annulene derivatives. *Nature Communications* **2017**, *8* (1), 346. DOI: 10.1038/s41467-017-00382-1.

(3) Frisch, M. J.; Trucks, G. W.; Schlegel, H. B.; Scuseria, G. E.; Robb, M. A.; Cheeseman, J. R.; Scalmani, G.; Barone, V.; Petersson, G. A.; Nakatsuji, H.; et al. Gaussian 16 Rev. B.01. **2016**.

(4) Mayer, Péter J.; Ottosson, H. False Identification of (Anti)aromaticity in Polycyclic Molecules in Ground and Excited States Through Incorrect Use of NICS. *Journal of Physical Organic Chemistry* **2025**, *38* (3). DOI: 10.1002/poc.70000.

(5) Gershoni-Poranne, R.; Stanger, A. Aromaticity: Modern Computational Methods and Applications. In *Aromaticity: Modern Computational Methods and Applications*, Fernández, I. Ed.; Elsevier, 2021; p Ch.4.

(6) Arpa, E. M.; Stafstrom, S.; Durbeej, B. HOMAc: A Parameterization of the Harmonic Oscillator Model of Aromaticity (HOMA) That Includes Antiaromaticity. *J Org Chem* **2025**, *90* (3), 1297-1308. DOI: 10.1021/acs.joc.4c02475.

(7) Geuenich, D.; Hess, K.; Köhler, F.; Herges, R. Anisotropy of the Induced Current Density (ACID), a General Method To Quantify and Visualize Electronic Delocalization. *Chemical Reviews* **2005**, *105* (10), 3758-3772. DOI: 10.1021/cr0300901.